



This is the accepted manuscript made available via CHORUS. The article has been published as:

Description of non-Darcy flows in porous medium systems

Amanda L. Dye, James E. McClure, Cass T. Miller, and William G. Gray

Phys. Rev. E **87**, 033012 — Published 18 March 2013

DOI: [10.1103/PhysRevE.87.033012](https://doi.org/10.1103/PhysRevE.87.033012)

Description of Non-Darcy Flows in Porous Medium Systems

Amanda L. Dye, Cass T. Miller, and William G. Gray
*Department of Environmental Sciences and Engineering,
University of North Carolina at Chapel Hill,
Chapel Hill, North Carolina 27599-7431*

James E. McClure
*Advanced Research Computing,
Virginia Tech, Blacksburg, Virginia 24061-0123*

Fluid flow through isotropic and anisotropic porous medium systems is investigated for a range of Reynolds numbers corresponding to both Darcy and non-Darcy regimes. A non-dimensional formulation is developed for a Forchheimer approximation of the momentum balance, and lattice Boltzmann simulations are used to elucidate the effects of porous medium characteristics on macroscale constitutive relation parameters. The geometric orientation tensor of the solid phase is posited as a morphological measure of leading-order importance for the description of anisotropic flows. Simulation results are presented to confirm this hypothesis, and parameter correlations are developed to predict closure relation coefficients as a function of porous medium porosity, specific interfacial area of the solid phase, and the geometric orientation tensor. The developed correlations provide improved estimates of model coefficients compared to available estimates and extend predictive capabilities to fully determine macroscopic momentum parameters for three-dimensional flows in anisotropic porous media.

I. INTRODUCTION

The equations that describe single-fluid-phase flow provide a fundamental basis for our understanding of the influence of the pore morphology and topology on momentum transport in porous media. Expressions such as Darcy's law and Forchheimer's equation describe flow processes in an averaged approximate sense, such that the complex microscopic structure typical of porous media can be effectively described using a small number of macroscopic parameters [1, 2]. The capacity to describe flow processes for a wide range of pore structures is contingent on our ability to identify and quantify the morphological and topological properties of a porous medium that are of leading order importance. Existing correlations predict parameters associated with approximations to the conservation of momentum equation using only the porosity and Sauter-mean diameter as the primary measures of porous medium morphology [3–5]. These correlations have been developed for restricted ranges of Reynolds numbers and porous medium morphologies. Furthermore, the available parametric correlations are insufficient to describe anisotropic systems where directional dependent effects impact the flow behavior. Proper mathematical description of anisotropy is essential to predict transport phenomena in many naturally occurring porous media.

The current state of knowledge categorizes single-fluid-phase flow into two primary regimes: a creeping flow regime corresponding to small flow velocities in which viscous forces completely dominate inertial forces, and a regime corresponding to flow velocities for which inertial forces cannot be neglected [6–10]. These two regimes are most commonly modeled by two approximations of the macroscale momentum equation for single-fluid-phase flow through a porous media: Darcy's law and Forchheimer's equation, respectively. The one-dimensional forms of these equations, which apply to isotropic flows, are familiar and have been studied extensively [1–3, 11–15]. More recent work has focused on deriving these traditional models for single-fluid-phase flow from first principles and linking macroscopic phenomena with microscopic flow behavior [6, 16–19]. Investigations have also linked the macroscopic permeability to tortuosity in both isotropic and anisotropic porous media [20–23]. While the anisotropic form of Darcy's law is relatively well-established, the proper form of the inertial correction term remains a matter of debate and predictive correlations for parameters in the anisotropic case are unavailable at present.

As details of porous medium micro-structure become increasingly accessible, opportunities exist to use this information to advance a more complete macroscopic understanding of flow through porous media. Computed microtomography techniques can provide three dimensional, high resolution images that reveal the pore-structure for a wide range of materials [24]. Numerical simulation techniques permit the study of increasingly large systems that can approach or exceed the size required for system properties to become size-independent provided that systems are homogeneous at the macroscale. The emergence of these technologies provides ample opportunities to exploit information collected in the field, such as imaging of core data. Most typically, properties such as the permeability and porosity are considered [25–27]. However, we suggest that the amount of predictive information that can be extracted from such data can be extended significantly based on current technology, particularly for anisotropic porous media.

The present state of knowledge is hindered by an incomplete understanding of non-Darcy flow in general at the macroscale, insufficient links between microscale porous medium morphology and anisotropic flow characteristics, and the lack of generally applicable estimations of parameters appearing in common flow equations. The development of the thermodynamically constrained averaging theory provides an opportunity to advance such descriptions by explicitly connecting spatial scales and identifying critical variables expected to affect single-fluid-phase flow [28]. This work will capitalize on that opportunity.

The primary objectives of this work are:

1. to develop a means to generate systematically isotropic and anisotropic porous medium systems with varying properties;
2. to perform highly resolved microscale simulations for a wide variety of porous medium systems at a scale that is sufficient to ensure a representative elementary volume (REV) for describing macroscale systems and hence the generality of the results;
3. to develop a formulation of the macroscale momentum resistance tensor that is consistent with microscale observations of anisotropic, non-Darcy flow behavior;
4. to identify porous medium characteristics that are of leading-order importance for determining parameter values appearing in macroscale equations used to describe fluid flow;
5. to derive an expression that can be used to relate media properties to macroscale flow parameters; and
6. to compare parameter correlations developed based upon this work with existing correlations.

II. BACKGROUND

A. Non-Darcy Flow

The three-dimensional momentum equation for single-phase flow in anisotropic porous media is approximated by [28]:

$$-\nabla p^w + \rho^w \mathbf{g}^{\overline{w}} = \hat{\mathbf{R}}^w \cdot \mathbf{v}^{\overline{w}} \quad (1)$$

where p^w is the volume-averaged fluid pressure of phase w , ρ^w is the volume-averaged mass density, $\mathbf{g}^{\overline{w}}$ is the mass-averaged gravitational acceleration vector, and $\mathbf{v}^{\overline{w}}$ is the mass-averaged velocity vector. The momentum resistance tensor $\hat{\mathbf{R}}^w$ must be symmetric and positive semi-definite to ensure that the entropy production is non-negative. We consider Eq. (1) written in the form

$$\psi |-\nabla p^w + \rho^w \mathbf{g}^{\overline{w}}| = \hat{\mathbf{R}}^w \cdot \boldsymbol{\omega} |\mathbf{v}^{\overline{w}}|. \quad (2)$$

Unit vectors provide the force orientation

$$\psi = \frac{-\nabla p^w + \rho^w \mathbf{g}^{\overline{w}}}{|-\nabla p^w + \rho^w \mathbf{g}^{\overline{w}}|}, \quad (3)$$

and flow orientation

$$\boldsymbol{\omega} = \frac{\mathbf{v}^{\overline{w}}}{|\mathbf{v}^{\overline{w}}|}. \quad (4)$$

Since ψ and $\boldsymbol{\omega}$ are dimensionless unit vectors, the dimensioned variables of importance can be identified as

$$|-\nabla p^w + \rho^w \mathbf{g}^{\overline{w}}| \quad [m/(l^2 t^2)], \quad (5)$$

$$|\mathbf{v}^{\overline{w}}| \quad [l/t], \quad (6)$$

$$\rho^w \quad [m/l^3], \quad (7)$$

$$\hat{\mu}^w \quad [m/(lt)], \quad (8)$$

$$\epsilon^{ws} \quad [1/l], \quad (9)$$

where $\hat{\mu}^w$ is the dynamic viscosity and ϵ^{ws} is the surface area of the ws interface per unit volume, which is equal to the specific interfacial area of the solid for this single-fluid-phase system. The surface-to-volume ratio is incorporated by using the Sauter mean diameter as the representative length scale for the flow

$$d = 6 \frac{\epsilon^s}{\epsilon^{ws}}, \quad (10)$$

where ϵ^s is the volume fraction of the solid phase.

For convenience, Eq. (2) can be arranged into a dimensionless form to simplify the task of analyzing parametric dependence on medium properties. Multiplying Eq. (2) by $\rho^w d^3 / (\hat{\mu}^w)^2$ leads to the expression

$$\psi F_c = \frac{d^2}{\hat{\mu}^w} \hat{\mathbf{R}}^w \cdot \boldsymbol{\omega} \text{Re}, \quad (11)$$

where the dimensionless forcing term is

$$F_c = \frac{\rho^w d^3 |-\nabla p^w + \rho^w \mathbf{g}^{\overline{w}}|}{(\hat{\mu}^w)^2} \quad (12)$$

and the Reynolds number is

$$\text{Re} = \frac{\rho^w d |\mathbf{v}^{\overline{w}}|}{\hat{\mu}^w}. \quad (13)$$

The momentum resistance tensor is symmetric and positive semi-definite and can be written in the form

$$\frac{d^2}{\hat{\mu}^w} \hat{\mathbf{R}}^w = \mathbf{Q}^w \cdot \boldsymbol{\Lambda}^w \cdot (\mathbf{Q}^w)^{-1}, \quad (14)$$

where the column vectors of \mathbf{Q}^w are a set of orthonormal eigenvectors of $\hat{\mathbf{R}}^w$, denoted by \mathbf{q}_i^w , $i = 1, 2, 3$. The diagonal tensor $\mathbf{\Lambda}^w$ contains the associated eigenvalues Λ_i^w . The eigenvectors of $\hat{\mathbf{R}}^w$ are assumed to be a property of the porous medium only.

The dependence of the momentum resistance on the flow velocity has been studied extensively for one-dimensional flows [2, 6, 8, 17, 18]. This dependence is introduced into the three-dimensional form by assuming that the eigenvalues Λ_i^w are a function of Re. For sufficiently small Re, a linear expansion can be applied to describe the flow behavior

$$\Lambda_i^w(\text{Re}) \approx \Lambda_i^a + \Lambda_i^b \text{Re}. \quad (15)$$

Based on this expansion the momentum resistance tensor takes the form

$$\frac{d^2}{\hat{\mu}^w} \hat{\mathbf{R}}^w = \mathbf{A} + \mathbf{B} \text{Re}, \quad (16)$$

where the Darcy momentum resistance tensor is

$$\mathbf{A} = \mathbf{Q}^w \cdot \mathbf{\Lambda}^a \cdot (\mathbf{Q}^w)^{-1}, \quad (17)$$

and the inertial momentum resistance tensor is

$$\mathbf{B} = \mathbf{Q}^w \cdot \mathbf{\Lambda}^b \cdot (\mathbf{Q}^w)^{-1}. \quad (18)$$

The diagonal tensors $\mathbf{\Lambda}^a$ and $\mathbf{\Lambda}^b$ provide the momentum resistance coefficients associated with the Darcy and non-Darcy flow effects. The diagonal values Λ_i^a specify the momentum resistance associated with \mathbf{q}_i^w within the Darcy regime and the diagonal values Λ_i^b account for the inertial correction that becomes important in the non-Darcy regime. While there are three independent components of \mathbf{v}^w the dependence on Re only considers the influence of the lone invariant quantity $|\mathbf{v}^w|$. The remaining two independent quantities are provided by the flow orientation $\boldsymbol{\omega}$. If \mathbf{A} and \mathbf{B} are independent of $\boldsymbol{\omega}$, Eq. (16) is a dimensionless form for the momentum resistance proposed by Wang et al. [20]. However, the directional-dependent flow behavior observed by McClure et al. suggests that the inertial momentum resistance tensor must also be a function of $\boldsymbol{\omega}$ for certain systems [29].

It would be advantageous to be able to predict \mathbf{A} and \mathbf{B} based on the knowledge of a small set of easily measured quantities. These tensors provide a macroscopic measure of the momentum resistance associated with a particular porous medium, and therefore depend on measures of the pore morphology and topology. In the dimensionless formulation this influence can be incorporated by identifying a set of dimensionless measures that can be functionally related to the components of \mathbf{A} and \mathbf{B} to produce predictive forms.

B. Correlations for Flow in Isotropic Porous Media

When the porous medium is isotropic, the tensors appearing in Eq. (16) must reduce to

$$\mathbf{A} = a^* \mathbf{I}, \quad (19)$$

$$\mathbf{B} = b^* \mathbf{I}, \quad (20)$$

where a^* and b^* are momentum resistance coefficients that apply for flows in isotropic porous media. Such flows can be described using the resulting one-dimensional counterpart to Eq. (11)

$$F_c = a^* \text{Re} + b^* \text{Re}^2. \quad (21)$$

The dependence of the coefficients a^* and b^* on porous medium morphology has been studied extensively [4, 5, 30–32]. With surface-to-volume effects accounted for by the length scale definition given in Eq. (10), existing correlations typically predict the coefficient values a^* and b^* as functions of the volume fraction of the w phase ϵ^w , or equivalently the porosity for this single-fluid-phase case, which is given by

$$\varepsilon = 1 - \epsilon^s. \quad (22)$$

The most well-known of these expressions is Ergun's equation, which specifies functional forms for the dimensionless permeability

$$a_e^* = \frac{\varepsilon^2}{\alpha_e^* (1 - \varepsilon)^2}, \quad (23)$$

and inertial coefficient

$$b_e^* = \beta_e^* \frac{(1 - \varepsilon)}{\varepsilon}. \quad (24)$$

Ergun [3] suggested that $\alpha_e^* = 150$ and $\beta_e^* = 1.75$, but several different values for the coefficients have been proposed. When $\alpha_e^* = 180$, Eq. (23) is the widely used Carman-Kozeny relationship [33]. MacDonald et. al. [5] determined that $1.8 \leq \beta_e^* \leq 4.0$ served to match experimental data from six different porous medium systems. For the case of Darcy flow, Rumpf and Gupte [4] predict the permeability using the relationship

$$a_{rg}^* = 5.6\varepsilon^{-5.5}. \quad (25)$$

Pan et. al. [32] found that the Carman-Kozeny relationship underestimates the permeability, and observed deviations from the Rumpf-Gupte relation when systems outside the range of experimental support for this expression were considered. They proposed an alternative correlation form in which an additional dimensionless variable, the relative standard deviation $\tilde{\sigma}_D$, was also included whereby

$$a_p^* = \alpha_{p1}^* \frac{\varepsilon^{\alpha_{p2}^*}}{\left(1 + \alpha_{p3}^* \tilde{\sigma}_D^{\alpha_{p4}^*}\right)}, \quad (26)$$

where α_{p1}^* , α_{p2}^* , α_{p3}^* and α_{p4}^* are best-fit coefficients.

III. METHODS

The objectives of this work will be accomplished using a simulation approach that relies upon the generation of a large set of isotropic and anisotropic porous medium systems with specified variations in size, shape, orientation, and porosity. The factors of leading-order importance for non-Darcy flow in anisotropic systems must first be posited and then evaluated and compared to simulation results. Simulations must be highly resolved microscale simulations of sufficient size to yield a reliable measure of a macroscale system. Each component of these methods is described in turn.

A. Generation of Sphere and Ellipsoid Packs

Surrogate porous media were constructed by generating sphere packs with log-normally distributed radii r_i . The sphere centroids, \mathbf{c}_i , $i = 1, 2, \dots, N_s$, were determined by a collective rearrangement algorithm designed for applications in porous media. The algorithm is a modified version of the one developed by Williams and Philipse to generate packs of sphereocylinders [34]. Our version of the algorithm is constructed to provide precise control over the final system porosity ε and to accommodate a lognormal size distribution for the sphere radii. Initially, a system of spheres is instantiated into a domain of fixed size. The initial sphere radii are assigned from a lognormal distribution with variance σ^2 and an initial mean μ_0 . The sphere centroids are initially distributed randomly based upon a uniform distribution throughout the domain, which is a rectangular prism with sides of length L_x , L_y and L_z . The initialization is summarized in the following pseudocode:

```

for  $i = 1, 2, \dots, N_s$  do
   $\log(r_i) \leftarrow \text{Normal}(\mu_0, \sigma^2)$ 
   $c_{i,x} \leftarrow \text{Uniform}(0, L_x)$ 
   $c_{i,y} \leftarrow \text{Uniform}(0, L_y)$ 
   $c_{i,z} \leftarrow \text{Uniform}(0, L_z)$ 
end for

```

The value of μ_0 is chosen so that the initial porosity is high based on the size of the system (in our case the initial porosity is $\varepsilon_0 = 0.80$). Once the initial system of spheres has been created, a collective rearrangement algorithm is applied to sequentially increase the size of the radii r_i using a constant rescaling factor λ , thereby decreasing ε until the desired porosity is reached. As the size of the radii are increased, the value of μ will increase and the system porosity will decrease. Each time the radii are rescaled an iterative procedure is applied to shift the sphere centroids so that all overlaps are eliminated. The direction to shift each sphere is determined by the overlap vector $\Delta \mathbf{x}_i$. The parameter κ was introduced in order to provide a way to tune the rate of convergence, which is increasingly important as σ^2 increases. This is due to the fact that sphere overlaps frequently occur between spheres of widely disparate

radii as σ^2 increases. A value of $\kappa = 0.6$ was sufficient for the systems considered in this work. However, it may be necessary to consider smaller values of κ to generate systems with larger values of σ^2 . The rescaling procedure is summarized in the following pseudocode:

```

while  $\sum_i \frac{4\pi r_i^3}{3} < (1 - \varepsilon) L_x L_y L_z$  do
   $r_i \leftarrow \lambda r_i$ 
   $\mu \leftarrow \mu + \log(\lambda)$ 
  while  $\max_{i,j} (|\mathbf{c}_i - \mathbf{c}_j| - r_i - r_j) > 1 \times 10^{-10}$  do
    for  $i = 1, 2, \dots, N_s$  do
       $\Delta \mathbf{x}_i = \sum_{j \neq i} [|\mathbf{c}_i - \mathbf{c}_j| - (r_i + r_j)] (\mathbf{c}_i - \mathbf{c}_j)$ 
    end for
    for  $i = 1, 2, \dots, N_s$  do
       $\mathbf{c}_i \leftarrow \mathbf{c}_i + \kappa \Delta \mathbf{x}_i$ 
    end for
  end while
end while

```

Full periodic boundary conditions are enforced, which eliminates the potential for boundary effects. For the homogeneous case $\sigma^2 = 0$ the minimum achievable porosity approaches 0.367, which is a well-established result for random close packs of equally-sized spheres [35, 36]. Lower porosity values become accessible as σ^2 increases. The variance σ^2 is specified as an input parameter, and is unchanged by the rescaling procedure. The final value of μ is determined from the desired porosity, which can be estimated using the equation

$$\varepsilon = 1 - \frac{4\pi N_s E[r_i^3]}{3L_x L_y L_z}, \quad (27)$$

where the expected value of the cube of the radius is

$$E[r_i^3] = \exp\left(3\mu + \frac{9}{2}\sigma^2\right). \quad (28)$$

Then, insertion of Eq. (28) into Eq. (27) and solution for μ yields

$$\mu = \frac{1}{3} \log\left(\frac{3(1 - \varepsilon) L_x L_y L_z}{4\pi N_s}\right) - \frac{3}{2}\sigma^2, \quad (29)$$

which relates the final mean radius for the lognormal distribution to the two independent input parameters ε and σ^2 .

The coordination number was used to evaluate the stability of each packing in a gravitational field. For a coordination number greater than six, the average number of spheres supporting each sphere is at least three. This threshold was used to establish an upper limit on the maximum porosity for a stable packing at a prescribed variance. The porosity ranges obtained for each variance are listed in Table I.

Variance (σ^2)	Porosity Range
0	0.37–0.60
0.1	0.35–0.54
0.2	0.32–0.48
0.3	0.30–0.42

TABLE I: Range of stable, accessible porosity values for log-normal sphere packs.

Anisotropic systems were constructed by applying the mapping $\{\eta x, \gamma y, \zeta z\} \rightarrow \{x', y', z'\}$ to sphere packs. In this work the stretch factors fall within the range of $1 \leq \eta, \gamma, \zeta \leq 1.7$. This procedure stretches the sphere packs to yield a system of axially-aligned ellipsoids. The resulting ellipsoid surfaces are given by the equation

$$\left(\frac{x' - c'_x}{\eta r}\right)^2 + \left(\frac{y' - c'_y}{\gamma r}\right)^2 + \left(\frac{z' - c'_z}{\zeta r}\right)^2 = 1. \quad (30)$$

where $\{c'_x, c'_y, c'_z\} = \{\eta c_x, \gamma c_y, \zeta c_z\}$. This mapping preserves both media porosity and grain contacts and can be used to generate a sequence of anisotropic media by considering different stretch factors η, γ and ζ applied to a given sphere

packing. While alternative algorithms exist to generate anisotropic media, this approach is advantageous due to the fact that each anisotropic packing is directly associated with an isotropic counterpart. Changes in the coefficient values can therefore be directly associated with changes in the system anisotropy with a minimum number of confounding factors.

B. The Orientation Tensor as a Quantitative Measure of Anisotropy

In order to extend the relationships developed for isotropic porous media to anisotropic systems, a dimensionless morphological measure of anisotropy must be identified and functionally related to \mathbf{A} and \mathbf{B} . In this work, we consider the average geometric orientation tensor [37] for the ws , or solid, surface as a quantitative measure of anisotropy

$$\mathbf{G}^{ws} = \frac{\int_{\Gamma_s} \mathbf{n}_s \mathbf{n}_s d\tau}{\int_{\Gamma_s} d\tau}, \quad (31)$$

where \mathbf{n}_s is the unit vector outward normal to the solid surface Γ_s .

The spectral decomposition of \mathbf{G}^{ws} provides a straightforward way to determine the anisotropic properties of a porous medium. The orientation tensor is symmetric and can be expressed in the form

$$\mathbf{G}^{ws} = \mathbf{Q}^s \cdot \boldsymbol{\Lambda}^s \cdot (\mathbf{Q}^s)^{-1}, \quad (32)$$

where orthonormal eigenvectors of \mathbf{G}^{ws} serve as the column vectors of \mathbf{Q}^s . The eigenvectors are denoted by \mathbf{q}_i^s , $i = 1, 2, 3$. The diagonal matrix $\boldsymbol{\Lambda}^s$ contains the associated eigenvalues Λ_i^s . Since \mathbf{n}_s is a unit vector, the first invariant of the orientation tensor places a constraint on the eigenvalues

$$\text{tr}(\mathbf{G}^{ws}) = \text{tr}(\boldsymbol{\Lambda}^s) = 1. \quad (33)$$

This implies that the tensor is uniquely specified according to two independent quantities and establishes that $\Lambda_1^s = \Lambda_2^s = \Lambda_3^s = 1/3$ for an isotropic system.

The eigenvectors provide the principal directions of anisotropy and the eigenvalues quantify the relative surface orientation associated with each eigenvector. The significance of these quantities is illustrated by the simple case of a rectangular prism. Consider a rectangular prism for which A_x , A_y and A_z denote the surface area of the x , y and z faces, respectively. Based on Eq. (31), the associated orientation tensor can be computed as

$$\mathbf{G}^{ws} = \frac{1}{A_x + A_y + A_z} \begin{bmatrix} A_x & 0 & 0 \\ 0 & A_y & 0 \\ 0 & 0 & A_z \end{bmatrix}. \quad (34)$$

For this geometry the eigenvectors align with the coordinate axes and the eigenvalues are

$$\Lambda_0^s = \frac{A_x}{A_x + A_y + A_z}, \quad (35)$$

$$\Lambda_1^s = \frac{A_y}{A_x + A_y + A_z}, \text{ and} \quad (36)$$

$$\Lambda_2^s = \frac{A_z}{A_x + A_y + A_z}. \quad (37)$$

Each eigenvalue Λ_i^s has the straightforward interpretation as the relative area of the part of the surface that has a normal vector aligned with \mathbf{q}_i^s .

Since Λ_i^s are dimensionless and provide a quantitative measure of anisotropy, it is natural to incorporate them into functional forms to predict the coefficients Λ_i^a and Λ_i^b . Furthermore, if \mathbf{q}_i^s can be used to approximate \mathbf{q}_i^w the momentum resistance tensor $\hat{\mathbf{R}}^w$ can be fully predicted using a small set of morphological information: ε , ϵ^{ws} and \mathbf{G}^{ws} . This posited leading-order dependency will be investigated through a series of highly resolved simulations.

C. Lattice Boltzmann Scheme

Simulations were carried out using a three-dimensional, nineteen velocity vector (D3Q19) multi-relaxation time (MRT) lattice Boltzmann (LB) scheme [38, 39]. The LB scheme recovers the Navier-Stokes equations to second order,

and is valid within both the Darcy and non-Darcy regimes. A solution for the pore-scale velocity field \mathbf{v}_w was obtained by simulating a steady state flow driven by an external force \mathbf{g}^w . Full periodic boundary conditions were used for all simulations, ensuring that $\nabla p^w = \mathbf{0}$. The density was given by $\rho^w = 1$ for all simulations. Prescribing \mathbf{g}^w in addition to the fluid viscosity $\hat{\mu}^w$ directly determines the value of Fc and ψ for each steady state simulation. Based on the microscale steady state velocity field, the macroscopic velocity was computed according to

$$\mathbf{v}^w = \frac{\int_{\Omega_w} \rho_w \mathbf{v}_w d\mathbf{r}}{\int_{\Omega_w} \rho_w d\mathbf{r}}. \quad (38)$$

The macroscopic velocity can be used to compute the Reynolds number according to Eq. (13), and ω may be computed from Eq. (4).

D. Determination of Representative Elementary Volumes

To ensure that the macroscopic results are independent of the domain size, each simulated system was large enough to be considered an REV. For the generated packing to be a valid REV, the resistance tensor must be independent of both the lattice size of the simulated domain and the packing size of the generated media.

Simulations were performed to generate flows for a sequence of $\text{Re} < 120$. The upper bound on Re was selected to ensure that a steady state was achieved. Higher values of Re lead to unsteady flows in which vortex shedding may occur. A least-squares fit of Eq. (21) was applied to the simulation data to obtain the corresponding values of a^* and b^* . To develop a porous medium that yielded grid-independent results, a system containing a set number of spheres was packed and the lattice size was increased until the resistance tensor converged to one definitive solution. This determined the number of lattice sites needed to resolve the mean grain diameter:

$$D = \exp \left[\mu + \frac{1}{2} \sigma^2 \right]. \quad (39)$$

The resulting parameter values are listed in Table II. Since the relative error for Eq. (21) was order 1×10^{-2} , it was determined that was an appropriate threshold to determine the REV for the purposes of this work. REV size was determined by incrementally increasing the number of spheres until the variation in the parameters a^* and b^* decreased below 1×10^{-2} , relative to the values a_∞^* and b_∞^* obtained at the highest resolution. The relative variation of these quantities are shown as functions of sphere number for each variance of lognormal distributed radii in Fig. 1. Table II outlines the number of spheres and cubic lattice sizes that define an REV porous medium for each variance of the log-normally distributed radii.

σ^2	N_s	n^3	D (pixels)
0	1500	360^3	33
0.1	1500	380^3	30
0.2	3000	460^3	28
0.3	4000	490^3	25

TABLE II: Domain sizes and resolution necessary to achieve a grid-independent REV.

IV. RESULTS AND DISCUSSION

A. Approximating the Eigenvectors of the Momentum Resistance Tensor

In order to produce useful parameter estimates for the anisotropic form of the momentum resistance tensor, the eigenvectors of $\hat{\mathbf{R}}^w$ must be associated with morphological properties of the solid phase. In an isotropic system every real-valued vector is an eigenvector of the momentum resistance tensor. This is readily apparent from Eq. (20). This is no longer the case for anisotropic systems. In anisotropic systems the eigenvectors \mathbf{q}_i^w correspond to those directions for which the force and flow orientations align. Identification of \mathbf{q}_i^w greatly simplifies the task of generating parameter estimates of $\hat{\mathbf{R}}^w$ since it reduces the number of undetermined parameters. Since the eigenvectors of \mathbf{G}^{ws} provide a way to identify principal directions of anisotropy in a given media, it is natural to relate them to the eigenvectors of $\hat{\mathbf{R}}^w$.

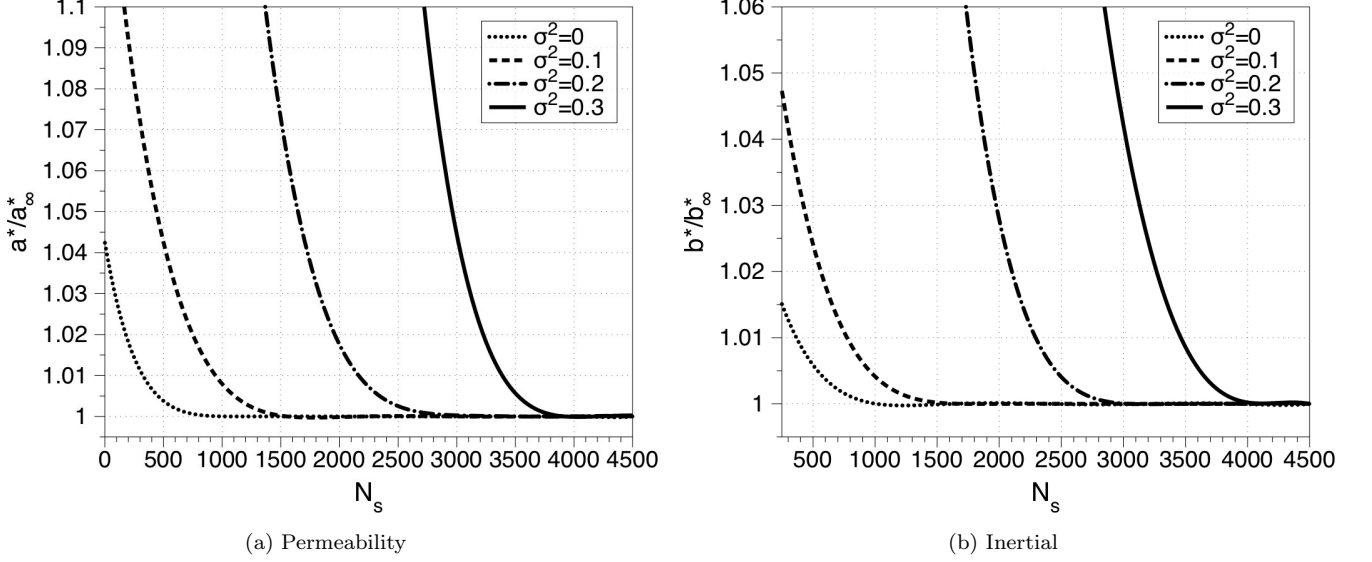


FIG. 1: Coefficient values relative to the associated REV obtained for a^* and b^* for a range of sphere packs.

The two-dimensional flows depicted in Fig. 2 provide physical insight into the significance of the eigenvectors in non-Darcy flows. In this case, the symmetry of the solid geometry ensures that eigenvectors of \mathbf{G}^{ws} align with the coordinate axes. When ψ aligns with one of these eigenvectors, the resulting flow orientation satisfies $\omega = \psi = \mathbf{q}_i^s$, as in Fig. 2 (a), (b), (d) and (e). The implication is that for this case the eigenvectors of \mathbf{G}^{ws} are also eigenvectors of $\hat{\mathbf{R}}^w$. Fig. 2 (c) and (f) demonstrate that ψ and ω will generally not be aligned in anisotropic systems.

Specifying the force orientation as $\psi = \mathbf{q}_i^s$ permits us to quantitatively evaluate if \mathbf{q}_i^s is an eigenvector of $\hat{\mathbf{R}}^w$ for a particular porous medium. The corresponding flow orientation ω can be obtained by simulating the steady state velocity field. If \mathbf{q}_i^s is an eigenvector of $\hat{\mathbf{R}}^w$, $\mathbf{q}_i^s \cdot \omega = 1$. The accuracy of the eigenvector approximation $\mathbf{q}_i^w \approx \mathbf{q}_i^s$ can therefore be evaluated by computing $|1 - \psi \cdot \omega|$. This error is plotted in Fig. 3 as a function of the Re. The properties of the associated ellipsoid packing were $\varepsilon = 0.38$, $\Lambda_0^s = 0.46$, $\Lambda_1^s = 0.25$ and $\Lambda_2^s = 0.29$. These results demonstrate that the eigenvectors of \mathbf{G}^{ws} provide an accurate way to identify the eigenvectors of $\hat{\mathbf{R}}^w$ for ellipsoid packs. The extensibility of this result to more general anisotropic media requires further study. Based on this approximation, we can write:

$$\mathbf{A} = \mathbf{Q}^s \cdot \boldsymbol{\Lambda}^a \cdot (\mathbf{Q}^s)^{-1}, \quad (40)$$

$$\mathbf{B} = \mathbf{Q}^s \cdot \boldsymbol{\Lambda}^b \cdot (\mathbf{Q}^s)^{-1}. \quad (41)$$

The task is thereby simplified to develop predictive relationships laws to approximate $\boldsymbol{\Lambda}^a$ and $\boldsymbol{\Lambda}^b$. Specific forms are presented in §IV E.

B. Dependence on the Flow Orientation

It has been known for over a century that the inertial correction to Darcy's law depends on the flow velocity [2, 3]. The precise form of this dependence has been the subject of ongoing study [20, 40, 41]. For one-dimensional flows, this dependence can be expressed in terms of Re without a loss of generality. For three-dimensional flows Re accounts for only the invariant of the velocity vector, $|\mathbf{v}^w|$, leaving two independent components unaccounted for. The remaining two independent components specify the flow orientation ω . Understanding how the momentum resistance depends on the flow orientation represents an important challenge to understanding flow processes in anisotropic porous media.

The dependence of the momentum resistance on Re is already established by Eq. (16). If the correction to Darcy's law is presumed to depend generally on \mathbf{v}^w , the implication is that \mathbf{B} is also a function of ω , of which only two components are independent. The first problem is that the components of ω are inherently determined by the coordinate system. Since the coordinate system is arbitrary, we must develop a way to study the impact of the flow orientation that is independent of this choice. Since the projection of the flow orientation onto the eigenvectors \mathbf{q}_i^s

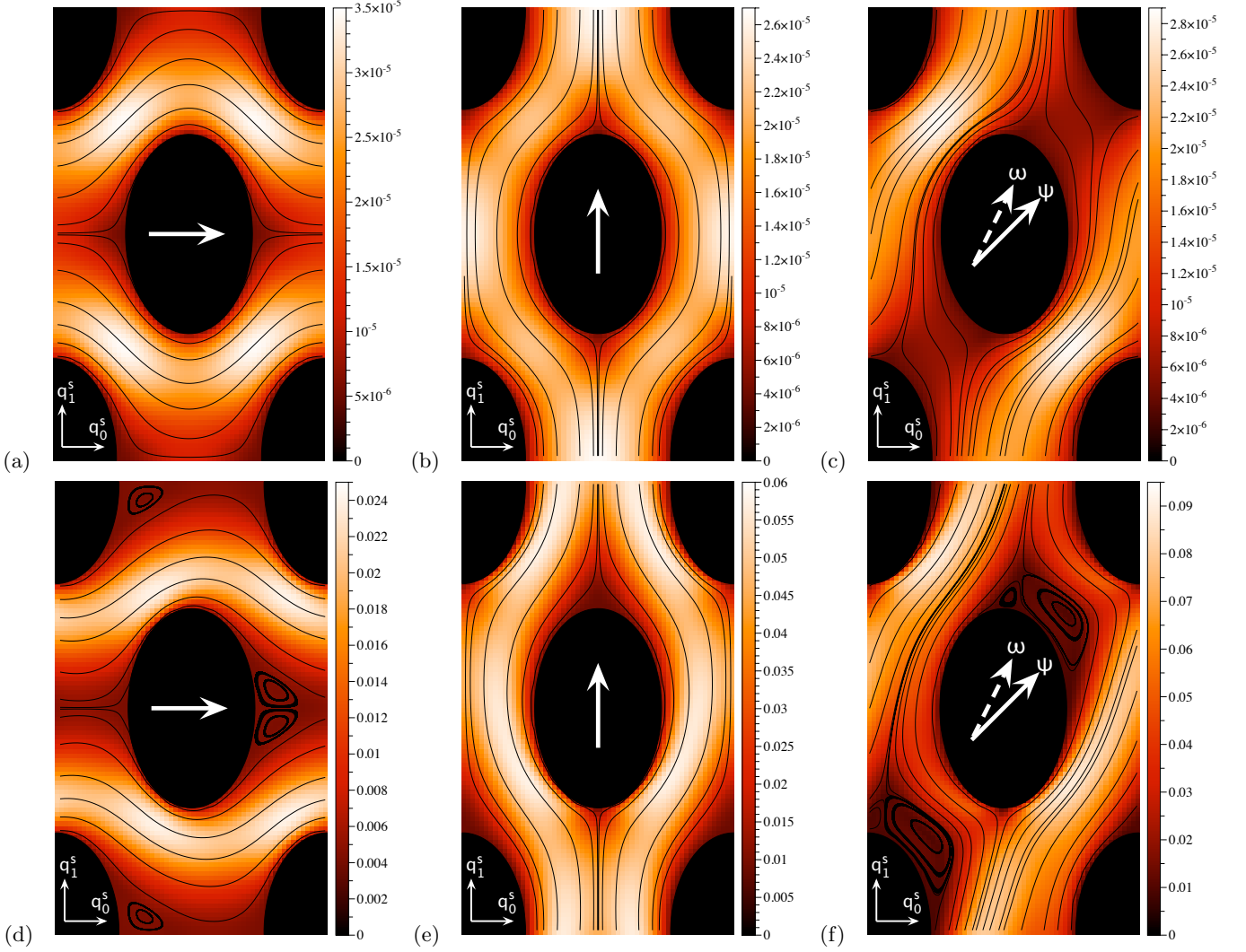


FIG. 2: (Color online) Streamlines resulting from Darcy (a–c) and non-Darcy (d–f) flows obtained using various force orientations in a simple periodic 2-D flow geometry. Darcy flows correspond to $\text{Re} = 0.01$ and non-Darcy flows correspond to $\text{Re} = 100$. The greyscale (color) value represents the magnitude of the flow velocity $|\mathbf{v}_w|$.

does not depend on the coordinate system, we will consider how $\mathbf{\Lambda}^b$ depends on the three quantities $\boldsymbol{\omega} \cdot \mathbf{q}_0^s$, $\boldsymbol{\omega} \cdot \mathbf{q}_1^s$ and $\boldsymbol{\omega} \cdot \mathbf{q}_2^s$.

Due to the fact that $\boldsymbol{\omega}$ has fixed unit length, a Taylor series cannot be applied to approximate the associated impact on the flow behavior. As a consequence, determining the functional dependence of \mathbf{B} on the flow orientation requires empiricism. However, the form of this dependence is subject to restrictions. First, in isotropic porous media Eq. (20) must be recovered for all possible flow orientations. Second, entropy production must be positive for all Re . In order to satisfy these constraints, we propose that the eigenvalues of \mathbf{B} can be predicted by the form:

$$\Lambda_i^b = \frac{\Lambda_i^{b(0)} |\boldsymbol{\omega} \cdot \mathbf{q}_0^s| + \Lambda_i^{b(1)} |\boldsymbol{\omega} \cdot \mathbf{q}_1^s| + \Lambda_i^{b(2)} |\boldsymbol{\omega} \cdot \mathbf{q}_2^s|}{|\boldsymbol{\omega} \cdot \mathbf{q}_0^s| + |\boldsymbol{\omega} \cdot \mathbf{q}_1^s| + |\boldsymbol{\omega} \cdot \mathbf{q}_2^s|}. \quad (42)$$

The coefficients $\Lambda_i^{b(j)}$ are functions of the porous medium morphology that determine the inertial contribution to momentum resistance in the direction of \mathbf{q}_i^s that results from a change in the projection of $\boldsymbol{\omega}$ on \mathbf{q}_i^s . A total of nine coefficients are necessary to specify \mathbf{B} in addition to the eigenvectors. The work of McClure et al. [29] suggests that $\Lambda_i^{b(j)}$ will also depend on the signed values of $\boldsymbol{\omega} \cdot \mathbf{q}_i^s$ for certain porous media. This possibility will not be explored in this work.

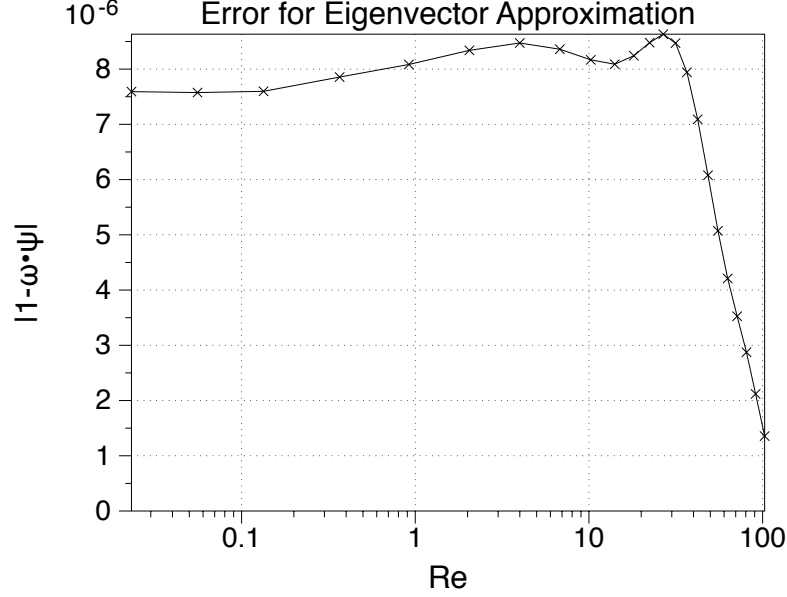


FIG. 3: Error for the approximation $\mathbf{q}_i^w \approx \mathbf{q}_i^s$ in an axially-aligned ellipsoid packing.

C. Physical Significance of Flow Coefficients and Eigenvectors

Recent work investigating the microscopic origins of inertial behavior in porous medium flows has linked the formation of eddies with macroscopic deviations from Darcy's law [7, 8, 29, 42]. This insight is particularly useful when attempting to understand the three-dimensional form given in Eq. (11). Eddies associated with the onset of inertial effects distort the flow field such that the resistance to flow increases. In anisotropic systems the size, shape, and location of these eddies differ depending on the flow orientation; and corresponding differences in the macroscopic flow behavior result. This effect is evident from considering the simple two-dimensional flows shown in Fig. 2. Three flow orientations were considered in a periodic flow domain, providing qualitative insight into the microscopic phenomena that must be accounted for by macroscopic coefficient values in anisotropic flows.

In Darcy flows, streamlines are independent of Re and invariant upon flow reversal, as shown in Fig. 2 (a–c). As a result the eigenvalues Λ_i^a are properties of the porous medium only. The three eigenvalues can be measured by conducting a set of three flow experiments in which flow orientations are aligned with each of the eigenvectors.

Inertial flows present a more challenging scenario; streamlines are no longer independent of Re as inertial effects begin to distort the flow field. For sufficiently high Re , the formation of eddies will be observed. The size, shape and position of these eddies depends both on Re and the flow orientation. Macroscopic coefficients must account for the impact that eddy formation has on the resulting flow behavior for all possible flow orientations. When the direction of ψ is aligned with one of the eigenvectors of \mathbf{G}^{ws} , as shown Fig. 2 (d) and (e), the eddies formed do not alter the eigenvectors of $\hat{\mathbf{R}}^w$. As a consequence, \mathbf{q}_i^w are presumed to be independent of Re .

The coefficients $\Lambda_i^{b(i)}$ determine the rate that momentum resistance increases due to the inertial distortions of the flow field that result when flow is aligned with \mathbf{q}_i^s . The coefficient $\Lambda_i^{b(j)}$, $j \neq i$ contributes to the momentum resistance only if $\omega \cdot \mathbf{q}_i^s$ and $\omega \cdot \mathbf{q}_j^s$ are both non-zero. These coefficient values provide a macroscopic measure of the momentum resistance caused by the varying size, shape and position of the eddies that form for different flow orientations. This picture is described qualitatively in Fig. 2 (f). A comparison of Fig. 2 (f) to Fig. 2 (d) and (e) reveals distinct qualitative differences between the flow fields. The necessity of the coefficients $\Lambda_i^{b(j)}$, $j \neq i$ can be assessed by considering their capacity to improve the accuracy of the estimated three-dimensional flow in an anisotropic porous medium.

The three-dimensional analog of Fig. 2 was used to evaluate the usefulness of Eq. (42). For simplicity, a symmetric geometry was selected to satisfy $\Lambda_1^s = \Lambda_2^s$. If \mathbf{B} is independent of ω only the three eigenvalues are needed to fully specify the form of the tensor, reducing to the form proposed by Wang et al. [20]. Flows aligned with the eigenvectors are sufficient to predict all three coefficients. In Fig. 4, flows aligned with eigenvectors \mathbf{q}_0^s and \mathbf{q}_1^s are labeled as Case A and Case B, respectively. The relative error of this approximation is determined by how well the quadratic form involving the Reynolds number matches the simulated data. In Case C, the flow orientation was selected to be

$(\mathbf{q}_0^s + \mathbf{q}_1^s)/2$. Based on the form of Wang et al. [20], Cases A and B provide all of the coefficients needed to predict the flow behavior in Case C. However, comparing the predicted and simulated data demonstrates that while this form predicts the flow behavior quite well in the Darcy regime, the relative error increases substantially with the onset of inertial effects at higher Re.

The implication of this result is that differences in location, size, and shape of eddies are dependent on the flow orientation; and these differences are manifested by a macroscopic difference in the flow behavior. To describe this flow behavior accurately, the inertial tensor \mathbf{B} must depend on $\boldsymbol{\omega}$. Flow data from Cases A, B, and C were then used to determine the associated coefficients, $\Lambda_0^a, \Lambda_1^a = \Lambda_2^a$ and $\Lambda_0^{b(0)}, \Lambda_0^{b(1)} = \Lambda_0^{b(2)}, \Lambda_1^{b(0)} = \Lambda_2^{b(0)}, \Lambda_2^{b(1)} = \Lambda_1^{b(2)}$, and $\Lambda_1^{b(1)} = \Lambda_2^{b(2)}$, where the equalities are implied by the symmetry of the flow geometry. The description of the inertial regime improves significantly when the effects of flow orientation are accounted for due to Eq. (42).

D. Parametric Estimates for Flow in Isotropic Porous Media

Simulations of non-Darcy flow were performed in isotropic sphere packs representing the full range of porosities and variances listed in Table I and $Re < 120$. Existing correlations for the dimensionless permeability and inertial parameter were then compared to these simulation results.

In Fig. 5, the simulation results of a specific isotropic case are shown. Based on simulated data points, the relative error is minimized for a^* and b^* based on Eq. (21). As a function of the Reynolds number, the relative error exhibits a similar profile for the isotropic case as compared to the anisotropic profile plotted in Fig. 4. Based on our analysis, the accuracy of Eq. (21) is within several percent. Since this is true for both isotropic and anisotropic cases, alternative forms which more accurately approximate the transition region from $1 < Re < 50$ would be a logical way to improve the predictive capabilities of this model. The consideration of such forms is beyond the scope of this work.

The functional forms listed in Eqs. (23)–(26) do not fully match the simulated data throughout the range of porosity values considered. This is unsurprising given that the range of porosity values considered here is broader than what has been considered in other studies. The Pan et al. [32] permeability relation was based on a set of flow simulations within a porosity range of $0.33 \leq \varepsilon \leq 0.45$. At the porosities outside the experimentally supported range, the Pan et al. [32] relation underestimates the measured permeability values, demonstrated in Fig. 6. The Carmen-Kozeny relation for lower porosities ($\varepsilon \leq 0.42$) underestimates the associated coefficient (Fig. 6). The lower porosity deviations are consistent with the findings of others [11, 13, 32, 43, 44]. The Rumpf-Gupte permeability relation deviates the most from the simulated data, over-predicting the data for $\varepsilon \geq 0.38$ and under-predicting for $\varepsilon \leq 0.38$. The Rumpf-Gupte data is based on flow experiments using sphere packs with relative standard deviations of the sphere-size distribution, $\tilde{\sigma}_D$, of 0.0945, 0.32, and 0.327 over a wide range of porosity ($0.366 \leq \varepsilon \leq 0.64$) and $0 < Re < 100$ [4, 5]. The cases with $\sigma^2 = 0.3$ and $0.36 < \varepsilon < 0.42$ are the only simulations that fit entirely within the experimentally supported regime of the Rumpf-Gupte relation. The data within the Rumpf-Gupte experiments correlates to the porosity range where deviations are a minimum, an observation supported by others [32, 43, 45].

We found that an exponential fit yields more satisfactory agreement for the full range of the simulation data. The associated functional form is:

$$a^*(\varepsilon) = \alpha_1^* \exp(\alpha_2^* \varepsilon), \quad (43)$$

where the best-fit coefficient values are $\alpha_1^* = 1.95 \times 10^{-5}$ and $\alpha_2^* = 9.85$ based on the simulated data points plotted in Fig. 6.

The inertial correction to Darcy's law is shown in Fig. 7. The coefficient b^* measured from simulation increases as porosity decreases. Simulated values for the inertial parameter are shown in comparison with values predicted by the Ergun functional form (Eq. (24)) in Fig. 7. Neither of the inertial coefficients predicted by Ergun or MacDonald provide a satisfactory fit to the simulation data; both relations over-predict the lower range of porosities (< 0.40) and under-predict the higher range of porosities (> 0.40). The Ergun relation was qualitatively based on a straight tube geometry of the pore space and has been found to be valid only in a range of Reynolds numbers, $0 \leq Re \leq 75$ [3, 5]. Based on the packing parameters set by the REV calculations (Table II), the range of Re simulated differs for each variance. The Reynolds number range is $0 \leq Re \leq 140$ for the homogenous packing ($\sigma^2 = 0$), $0 \leq Re \leq 130$ for $\sigma^2 = 0.1$, $0 \leq Re \leq 115$ for $\sigma^2 = 0.2$, and $0 \leq Re \leq 95$ for $\sigma^2 = 0.3$. As the Re range for each variance increases past the upper Re limit of the Ergun relation, the difference between the simulated data and the inertial parameters predicted by Ergun increases. The Ergun relation has also been found to be valid only for $0.38 \leq \varepsilon \leq 0.47$ [46].

The Ergun relation matches the simulated data well within the restricted range before diverging at a porosity of 0.35. The MacDonald et al. relation is the Ergun relation (Eq. (24)) with a modified $\hat{\beta}_e^*$ coefficient based on the comparative analysis of numerous experimental results, including the data of Rumpf and Gupta. The analysis took into account data from a wide range of porosities ($0.123 \leq \varepsilon \leq 0.919$) and granular shapes and sizes with the goal

of deriving an Ergun relation that was applicable for packs of non-spherical grains [5]. Much of the lower porosity data ($\varepsilon \leq 0.40$) came from experiments using irregularly shaped objects, sand and gravel mixtures, and a variety of undisclosed materials. Since the simulated data only takes into account porous media composed of smooth spheres, roughness could explain the large deviations between the inertial parameter predicted by the MacDonald et al. relation and the simulated data at $\varepsilon \leq 0.40$.

To provide a better fit for the full range of simulated data, an alternative functional form is proposed to provide a better match of the simulated data:

$$b^*(\varepsilon) = \beta_1^* \frac{(1 - \varepsilon)^{\beta_2^*}}{\varepsilon^{\beta_3^*}}. \quad (44)$$

where the coefficients $\beta_1^* = 4.21$, $\beta_2^* = 1.58$ and $\beta_3^* = 0.378$ were obtained by performing a least squares analysis to minimize the relative error based on the simulated data points shown in Fig. 7.

E. Parametric Estimates for Flow in Anisotropic Porous Media

The results of §IV D establish functional forms that predict the values of flow coefficients in an isotropic system as a function of the media porosity, expanding on the results of prior studies. In this section, extended correlations are developed that apply to systems where anisotropic effects contribute to the flow behavior.

To resolve the flow behavior in anisotropic porous media, six different force orientations were used. These orientations corresponded to $[1, 0, 0]^T$, $[0, 1, 0]^T$, $[0, 0, 1]^T$, $[\sqrt{2}, \sqrt{2}, 0]^T$, $[\sqrt{2}, 0, \sqrt{2}]^T$, $[0, \sqrt{2}, \sqrt{2}]^T$. Between 100 and 150 steady state simulations were performed for each anisotropic medium. Each steady state simulation corresponded to values of ψ , ω , Fc and Re that were used to determine all coefficient values for the media. Based on Eqs. (40)–(41), twelve coefficients are necessary, in addition to the eigenvectors \mathbf{q}_i^s , to fully specify the macroscopic flow behavior. These coefficients were calculated by performing a non-linear least squares approach to minimize

$$\Phi_i = \sum_{\{\text{Re}, \text{F}, \omega, \psi\}} \left[\psi \cdot \mathbf{q}_i^s - \frac{1}{\text{F}} \left(\Lambda_i^a \text{Re} + \frac{\sum_j \Lambda_i^{b(j)} |\mathbf{q}_i^s \cdot \omega|}{\sum_j |\mathbf{q}_j^s \cdot \omega|} \text{Re}^2 \right) \omega \cdot \mathbf{q}_i^s \right]^2, \quad (45)$$

where the index $i = 0, 1, 2$ specifies the eigenvectors associated with the principal directions of anisotropy. The full set of coefficients were determined by numerical solution of a set of the non-linear equations

$$\frac{\partial \Phi_i}{\partial \Lambda_i^a} = 0 \text{ for } i = 0, 1, 2, \quad (46)$$

$$\frac{\partial \Phi_i}{\partial \Lambda_i^{b(j)}} = 0 \text{ for } i, j = 0, 1, 2. \quad (47)$$

Simulations were performed using a large number of media to obtain a well-resolved range of anisotropies as shown in Fig. 8. Based on these simulations flow coefficients were determined for each medium using Eqs. (46)–(47). Specific functional forms accounting for anisotropy were then selected to match the simulation data.

Since each ellipsoid pack is defined by the mapping procedure given in Eq. (30), we can understand anisotropic effects by considering how the introduction of anisotropy alters the flow coefficients for a given sphere pack. In practice, each sphere pack exhibits a small amount of anisotropy as determined by the accuracy of the REV. We account for this by measuring the full set of coefficients for each sphere pack, which we denote by Λ_i^{a*} and $\Lambda_i^{b(j)*}$. The coefficient values from an ellipsoid packing can then be compared to these values to more accurately determine the associated impact on flow behavior. The components of \mathbf{G}^{ws} were determined numerically for the anisotropic systems considered in this work.

Predictive functional forms for Λ_i^a and Λ_i^b were developed by constructing separable functions to account for each independent variable. Because of the constraint of Eq. (33), two functions are sufficient to fully describe the influence of \mathbf{G}^{ws} . Since the indexing of the eigenvectors \mathbf{q}_i^s is non-unique, the constitutive functions must be identical for all permutations of the index convention. The eigenvalue Λ_i^s , which provides a measure of the relative blockage orthogonal to \mathbf{q}_i^s , was selected as the first of these values. Since the labeling of the remaining axes is arbitrary, the additional quantity obtained from the orientation tensor must be symmetric with respect to Λ_j^s and Λ_k^s . This is satisfied by choosing the second independent quantity to be $|\Lambda_j - \Lambda_k|$. We then search for constitutive relationships of the form

$$\Lambda_i^a = a^*(\varepsilon) a^\parallel(\Lambda_i^s) a^\perp(|\Lambda_j^s - \Lambda_k^s|), \quad i \neq j \neq k, \quad (48)$$

$$\Lambda_i^{b(i)} = b^*(\varepsilon) b^\parallel(\Lambda_i^s) b^\perp(|\Lambda_j^s - \Lambda_k^s|), \quad i \neq j \neq k. \quad (49)$$

The functional forms $a^{\parallel}, a^{\perp}, b^{\parallel}$ and b^{\perp} must equal unity for an isotropic system (ie. $\Lambda_i^s = \frac{1}{3}$ and $|\Lambda_j^s - \Lambda_k^s| = 0$), which is satisfied by the subsequent expressions given in Eqs. (50)–(53).

Simulation results indicate that Λ_i^s is responsible for the largest part of the anisotropic correction to Λ_i^a and Λ_i^b . In order to match the simulation data, the constitutive laws were formulated as

$$a^{\parallel}(\Lambda_i^s) = \left[1 + \alpha_1^{\parallel} \left(\Lambda_i^s - \frac{1}{3} \right) \right]^{\alpha_2^{\parallel}}, \quad (50)$$

$$b^{\parallel}(\Lambda_i^s) = \left[1 + \beta_1^{\parallel} \left(\Lambda_i^s - \frac{1}{3} \right) \right]^{\beta_2^{\parallel}}. \quad (51)$$

The best fit coefficients are $\alpha_1^{\parallel} = 1.40$, $\beta_1^{\parallel} = 0.351$, $\alpha_2^{\parallel} = 1.06$, and $\beta_2^{\parallel} = 11.1$. To obtain these coefficients, systems were constructed such that $\Lambda_j^s = \Lambda_k^s$ for $k \neq j \neq i$. Plots of the simulation data and resulting functions are shown in Fig. 9.

A smaller contribution is associated with $|\Lambda_j^s - \Lambda_k^s|$. A linear functional form was selected to account for this contribution

$$a^{\perp}(|\Lambda_j^s - \Lambda_k^s|) = 1 + \alpha^{\perp} |\Lambda_j^s - \Lambda_k^s|, \quad (52)$$

and

$$b^{\perp}(|\Lambda_j^s - \Lambda_k^s|) = 1 + \beta^{\perp} |\Lambda_j^s - \Lambda_k^s|. \quad (53)$$

The best-fit coefficients were $\alpha^{\perp} = 0.0173$ and $\beta^{\perp} = 0.229$. The range of porosity values and variances considered to obtain these results are summarized in Table I and the range of orientation tensor eigenvalues are plotted in Fig. 8. Since $a^{\perp}(0) = 1$ and $b^{\perp}(0) = 1$, the anisotropic contribution disappears when an isotropic system is considered. As demonstrated by Fig. 10, the contribution of a^{\perp} and b^{\perp} is the approximately the same order of magnitude as the error contribution. Not coincidentally, this error is the same order of magnitude as the error in the quadratic form for the Non-Darcy momentum resistance, shown in Fig. 4. Based on this, we conclude that the inclusion of a^{\perp} and b^{\perp} are unlikely to improve the description significantly. Alternatively, a^{\perp} and b^{\perp} could be set to 1, their values for an isotropic system, for simplicity.

The remaining inertial coefficients, $\Lambda_i^{b(j)}$, $i \neq j$, contribute only when the flow is not aligned with one of the eigenvectors \mathbf{q}_i^s . Parameter values for these coefficients presumed that these coefficients could be described by

$$\Lambda_i^{b(j)} = b^*(\varepsilon) b^{\dagger}(\Lambda_i^s - \Lambda_j^s) b^{\ddagger}(\Lambda_k^s) \quad (54)$$

The coefficient $\Lambda_i^{b(j)}$ provides the relative change to the momentum resistance in the direction of \mathbf{q}_i^s that results from a change in

$$b^{\dagger}(\Lambda_i^s - \Lambda_j^s) = \exp [\beta^{\dagger}(\Lambda_i^s - \Lambda_j^s)], \quad (55)$$

$$b^{\ddagger}(\Lambda_k^s) = \exp \left[\beta^{\ddagger} \left(\Lambda_k^s - \frac{1}{3} \right) \right], \quad (56)$$

where $\beta^{\dagger} = 0.742$ and $\beta^{\ddagger} = -2.05$. A plot of the resulting functional form is shown in Fig. 11.

The anisotropic parameter correlations given in Eqs. (50)–(56) combine with the results of §IV D to provide a complete set of predictive coefficients for Eq. (11) for any system where the porosity, specific surface area, and orientation tensor are known. The functional forms proposed to account for these various contributions are summarized in Table III. Several basic principles were relied upon to produce these relationships, which are summarized as follows:

1. The eigenvalues of the tensors **A** and **B** are each non-negative to ensure that the second law of thermodynamics is satisfied for all Reynolds numbers.
2. By constructing the formulation in terms of the eigendecomposition of the momentum resistance tensor and identifying the associated eigenvectors, the description is fully independent of the coordinate system choice.
3. The tensor form of the momentum transport equation reduces exactly to the one-dimensional form given in Eq. (21) if the solid surface is isotropic ($\Lambda_i^s = \frac{1}{3}$).

Specific functional forms were selected to satisfy these constraints while matching the simulated data as closely as possible.

Microscopic imaging techniques can be exploited to obtain direct measurements of both surface area and orientation tensor values. When working with such data, a spectral decomposition must be applied to the numerically computed orientation tensor \mathbf{G}^{ws} to obtain \mathbf{q}_i^s and Λ_i^s . Our results suggest that the eigenvectors of \mathbf{G}^{ws} provide a good approximation for the eigenvectors of \mathbf{A} and \mathbf{B} . Since our results were obtained for systems of axially-aligned ellipsoids, future studies should consider the extensibility of these results to more general anisotropic porous media. However, the use of dimensionless variables should facilitate the extension of these results to a wide range of systems. Since the surface area and orientation tensor can be constructed easily based on computed micro-tomography data, this would seem to present a natural opportunity to examine the extensibility of these results to more general anisotropic porous media. It is possible that other dimensionless morphological measures exert influence on momentum transport for certain systems, and the identification of such measures present additional opportunities to expand the predictive capabilities for non-Darcy flows beyond the leading-order factors identified herein.

Parameter	Dependence	Functional Form	Coefficient Values
Λ_i^a	$a^*(\varepsilon)$	$\alpha_1^* \exp(\alpha_2^* \varepsilon)$	$\alpha_1^* = 1.95 \times 10^{-5}, \alpha_2^* = 9.85$
Λ_i^a	$a^\parallel(\Lambda_i^s)$	$\left[1 + \alpha_1^\parallel \left(\Lambda_i^s - \frac{1}{3}\right)\right]^{\alpha_2^\parallel}$	$\alpha_1^\parallel = 1.40, \alpha_2^\parallel = 1.06$
Λ_i^a	$a^\perp(\Lambda_j^s - \Lambda_k^s)$	$1 + \alpha^\perp \Lambda_j^s - \Lambda_k^s $	$\alpha^\perp = 0.0173$
$\Lambda_i^{b(i)}, \Lambda_i^{b(j)}$	$b^*(\varepsilon)$	$\beta_1^* \frac{(1-\varepsilon)^{\beta_2^*}}{\varepsilon^{\beta_3^*}}$	$\beta_1^* = 4.21, \beta_2^* = 1.58, \beta_3^* = 0.378.$
$\Lambda_i^{b(i)}$	$b^\parallel(\Lambda_i^s)$	$\left[1 + \beta_1^\parallel \left(\Lambda_i^s - \frac{1}{3}\right)\right]^{\beta_2^\parallel}$	$\beta_1^\parallel = 0.351, \beta_2^\parallel = 11.1$
$\Lambda_i^{b(i)}$	$b^\perp(\Lambda_j^s - \Lambda_k^s)$	$1 + \beta^\perp \Lambda_j^s - \Lambda_k^s $	$\beta^\perp = 0.229$
$\Lambda_i^{b(j)}$	$b^\dagger(\Lambda_i^s - \Lambda_j^s)$	$\exp\left[\beta^\dagger (\Lambda_i^s - \Lambda_j^s)\right]$	$\beta^\dagger = 0.742$
$\Lambda_i^{b(j)}$	$b^\ddagger(\Lambda_k^s)$	$\exp\left[\beta^\ddagger \left(\Lambda_k^s - \frac{1}{3}\right)\right]$	$\beta^\ddagger = -2.05$

TABLE III: Summary of the functional forms and coefficient values proposed to predict momentum equation parameters ($i \neq j \neq k$). The tensors \mathbf{A} and \mathbf{B} can be determined by combining these expressions with Eqs. (48)–(49), Eq. (54) and Eqs. (40)–(41).

V. SUMMARY AND CONCLUSIONS

In this work, a large set of lattice Boltzmann simulations were performed to produce constitutive relationships that fully predict all coefficients required to close a tensorial form of the momentum transport equations for single-phase flow in porous media. Essential closure information for both isotropic and anisotropic flows in porous media is provided as a function of nondimensional measures of the porous medium morphology. In the isotropic case, simulated data was compared to existing relationships including those due to Ergun, Rumpf and Gupta, MacDonald et al., Carmen-Kozeny, and Pan et al. As shown in our work, these equations have varying degrees of accuracy in their application, depending on the quantity and quality of the data used to derive them. Our work improves upon these existing correlations by considering data for a wider range of morphological and flow characteristics than previously examined. We also studied the dependence of single-fluid-phase flow through anisotropic media on morphological characteristics beyond porosity and postulated a quantitative measure of anisotropy that we demonstrated to be predictive of the macroscopic flow behavior. This result is significant because it concretely establishes a connection between the macroscopic flow coefficients and an averaged measure of the anisotropy of underlying solid phase morphology: the orientation tensor. As a consequence, the predictive capabilities for anisotropic flows are extended significantly. A summary of the major contributions of this work are as follows:

1. A collective rearrangement algorithm and mapping procedure was developed to generate packed periodic systems of spheres and ellipsoids that matched a specified porosity and size distribution.
2. An approach was derived to simulate highly resolved flows that were essentially grid independent for a representative elementary volume of porous medium systems and guidance was given on how such systems can be created.
3. The momentum resistance of non-Darcy flows was demonstrated to depend linearly on the Reynolds number and non-linearly on the flow orientation, accounting for all three independent components of the flow velocity. An empirical form was introduced to account for the influence of the flow orientation in anisotropic flows.

4. Porosity, specific interfacial area, and the geometric orientation of the solid surface were shown to be the variables of leading-order importance in assessing Darcy and non-Darcy single-fluid-phase flow through anisotropic porous media.
5. The spectral decomposition of the momentum resistance tensor was studied and an approach was proposed to predict both the eigenvectors and eigenvalues. An empirical functional form was posited to represent the momentum resistance tensor and correlations were developed to predict parameter values based upon a large number of highly resolved simulations.
6. The functional form developed in this work to predict the resistance tensor was compared to available estimates and shown to be significantly more accurate than previous estimates when the entire range of simulations performed in this work was examined.

ACKNOWLEDGEMENTS

This work was supported by National Science Foundation grant ATM-0941235 and Department of Energy grant DE-SC0002163x.

-
- [1] H. Darcy. *Les Fontaines Publiques de la Ville de Dijon*. Dalmont, Paris, 1856.
 - [2] P. H. Forchheimer. Wasserbewegung durch boden. *Zeitschrift des Vereines Deutscher Ingenieure*, 45:1782–1788, 1901.
 - [3] S. Ergun. Fluid flow through packed columns. *Chemical Engineering Progress*, 48:89–94, 1952.
 - [4] H. Rumpf and A. R. Gupta. Einflüsse der Porosität und Korngrößenverteilung im Widerstandsgesetz der Porenströmung. *Chemie Ingenieur Technik*, 43:367–375, 1971.
 - [5] Mow K. Dullien F. Macdonald F., El-Sayed S. Flow through porous media - the ergun equation revisited. *Ind. Eng. Chem. Fundam.*, 18(3):199–208, 1979.
 - [6] H. Ma and D. W. Ruth. A numerical-analysis of the interfacial drag force for fluid-flow in porous-media. *Transport in Porous Media*, 17(1):87–103, 1994.
 - [7] M. Fourar, G. Radilla, R. Lenormand, and C. Moyne. On the non-linear behavior of a laminar single-phase flow through two and three-dimensional porous media. *Advances in Water Resources*, 27(6):669–677, 2004.
 - [8] M. Panfilov and M. Fourar. Physical splitting of nonlinear effects in high-velocity stable flow through porous media. *Advances in Water Resources*, 29(1):30–41, 2006.
 - [9] M. Bayani Cardenas. Three-dimensional vortices in single pores and their effects on transport. *Geophysical Research Letters*, 35(18), SEP 17 2008.
 - [10] Kuldeep Chaudhary, M. Bayani Cardenas, Wen Deng, and Philip C. Bennett. The role of eddies inside pores in the transition from Darcy to Forchheimer flows. *Geophysical Research Letters*, 38, DEC 30 2011.
 - [11] J. P. du Plessis and J. H. Masliyah. Mathematical modelling of flow through consolidated isotropic porous media. *Transport in Porous Media*, 3(2):145–161, 1988.
 - [12] J. P. du Plessis. High reynolds number flow through granular porous media. In T. F. Russell, R. E. Ewing, C. A. Brebbia, W. G. Gray, and G. F. Pinder, editors, *Mathematical Modeling in Water Resources*, volume 2, pages 179–186, Denver, 1992. Computational Mechanics Publications.
 - [13] J. P. Duplessis. Analytical quantification of coefficients in the Ergun equation for fluid friction in a packed-bed. *Transport in Porous Media*, 16(2):189–207, 1994.
 - [14] S. J. Liu and J. H. Masliyah. Single fluid flow in porous media. *Chemical Engineering Communications*, 150:653–732, 1996.
 - [15] S. Liu and J. H. Masliyah. Principles of single-phase flow through porous media. In L. L. Schramm, editor, *Suspensions: Fundamentals and Applications in the Petroleum Industry*, volume 251, pages 227–286. American Chemical Society, Washington, 1996.
 - [16] S. Whitaker. Flow in porous media I: A theoretical derivation of Darcy’s law. *Transport in Porous Media*, 1:3–25, 1986.
 - [17] S. M. Hassanizadeh and W. G. Gray. High-velocity flow in porous-media. *Transport in Porous Media*, 2(6):521–531, 1987.
 - [18] S. M. Hassanizadeh and W. R. Gray. Reply to comments by Barak on ‘High velocity flow in porous media’ by Hassanizadeh and Gray. *Transport in Porous Media*, 3(3):319–321, 1988.
 - [19] D. Ruth and H. P. Ma. On the derivation of the Forchheimer equation by means of the averaging theorem. *Transport in Porous Media*, 7(3):255–264, 1992.
 - [20] X. Wang, F. Thauvin, and K. K. Mohanty. Non-Darcy flow through anisotropic porous media. *Chemical Engineering Science*, 54(12):1859–1869, 1999.
 - [21] Peijun Guo. Dependency of Tortuosity and Permeability of Porous Media on Directional Distribution of Pore Voids. *Transport in Porous Media*, 95(2):285–303, NOV 2012.
 - [22] Bettina Albers and Krzysztof Wilmanski. Acoustics of two-component porous materials with anisotropic tortuosity. *Continuum Mechanics and Thermodynamics*, 24(4-6, SI):403–416, NOV 2012.

- [23] S. A. Galindo-Torres, A. Scheuermann, and L. Li. Numerical study on the permeability in a tensorial form for laminar flow in anisotropic porous media. *Physical Review E*, 86(4, Part 2), OCT 10 2012.
- [24] M. Prodanovic, W. B. Lindquist, and R. S. Seright. 3D image-based characterization of fluid displacement in a Berea core. *Advances in Water Resources*, 30(2, SI):214–226, FEB 2007. Meeting on Pore-Scale Modelling, Chapel Hill, NC, 2004.
- [25] Francois Renard, Dominique Bernard, Jacques Desrues, and Audrey Ougier-Simonin. 3D imaging of fracture propagation using synchrotron X-ray microtomography. *Earth and Planetary Science Letters*, 286(1-2):285–291, AUG 30 2009.
- [26] N. Watanabe, T. Ishibashi, N. Hirano, N. Tsuchiya, Y. Ohsaki, T. Tamagawa, Y. Tsuchiya, and H. Okabe. Precise 3D Numerical Modeling of Fracture Flow Coupled With X-Ray Computed Tomography for Reservoir Core Samples. *SPE Journal*, 16(3):683–691, SEP 2011.
- [27] A. Ja’fari and Moghadam R. Integration of ANFIS, NN and GA to determine core porosity and permeability from conventional well log data. *Journal of Geophysics and Engineering*, 9(5):473–481, OCT 2012.
- [28] W. G. Gray and C. T. Miller. Thermodynamically constrained averaging theory approach for modeling flow and transport phenomena in porous medium systems: 3. Single-fluid-phase flow. *Advances in Water Resources*, 29(11):1745–1765, 2006.
- [29] J. E. McClure, W. G. Gray, and C. T. Miller. Beyond Anisotropy: Examining Non-Darcy Flow in Asymmetric Porous Media. *Transport in Porous Media*, 84(2):535–548, SEP 2010.
- [30] M. R. Tek. Development of a generalized Darcy equation. *Trans AIME*, 210:376–377, 1957.
- [31] J. Geertsma. Estimating the coefficient of inertial resistance in fluid flow through porous media. *Soc. Petrol. Eng.*, pages 211–216, October 1974.
- [32] C. Pan, M. Hilpert, and C. T. Miller. Pore-scale modeling of saturated permeabilities in random sphere packings. *Physical Review E*, 64(6):9, 2001.
- [33] J. Bear. *Dynamics of Fluids in Porous Media*. Elsevier, New York, 1972.
- [34] S. Williams and A. Philipse. Random packings of spheres and spherocylinders simulated by mechanical contraction. *Physical Review E*, 67, 2003.
- [35] W. S. Jodrey and E. M. Tory. Computer simulation of close random packing of equal spheres. *Physical Review A*, 32(4):2347–2351, 1985.
- [36] A. S. Clarke and J. D. Wiley. Numerical simulation of the dense random packing of a binary mixture of hard spheres: Amorphous metals. *Physical Review B*, 35(14):7350–7356, 1987.
- [37] W. G. Gray, A. F. B. Tompson, and W. E. Soll. Closure conditions for two-fluid flow in porous media. *Transport in Porous Media*, 47(1):29–65, 2002.
- [38] D. d’Humières, I. Ginzburg, M. Krafczyk, P. Lallemand, and L. S. Luo. Multiple-relaxation-time lattice Boltzmann models in three dimensions. *Philosophical Transactions of the Royal Society of London Series A-Mathematical Physical and Engineering Sciences*, 360:437–451, 2002.
- [39] C. Pan, L.-S. Luo, and C. T. Miller. An evaluation of lattice Boltzmann schemes for porous medium flow simulation. *Computers & Fluids*, 35(8–9):898–909, 2006.
- [40] V. D. Cvetcovic. A Continuum Approach to High-Velocity Flow in a Porous Medium. *Transport in Porous Media*, 1(1):63–97, 1986.
- [41] M. Firdaouss, J. L. Guermont, and P. LeQuere. Nonlinear corrections to Darcy’s law at low reynolds numbers. *Journal of Fluid Mechanics*, 343:331–350, 1997.
- [42] M. Fourar and R. Lenormand. A new model for two-phase flows at high velocities through porous media and fractures. *Journal of Petroleum Science and Engineering*, 30(2):121–127, 2001.
- [43] F. A. L. Dullien. *Porous Media: Fluid Transport and Pore Structure*. Academic Press, San Diego, CA, 1979.
- [44] J. P. du Plessis and J. H. Masliyah. Flow through isotropic granular porous media. *Transport in Porous Media*, 6:207–221, 1991.
- [45] Barnea E. and R. L. Mednick. A generalized approach to the fluid dynamics of particulate systems part iii: General correlation for the pressure drop through fixed beds of spherical particles. *The Chemical Engineering Journal*, 15.2:215–227, 1978.
- [46] J. Happel and H. Brenner. *Low Reynolds Number Hydrodynamics*. Prentice-hall, Englewood Cliffs, NJ, 1965.
- [47] M. Rasoloarijaona and J. L. Auriault. Nonlinear seepage flow-through a rigid porous-medium. *European Journal of Mechanics B-Fluids*, 13(2):177–195, 1994.
- [48] P. du Plessis and L. I. Roos. Predicting the hydrodynamic permeability of sandstone with a pore-scale model. *Journal of Geophysical Research*, 99(B10):19,771–19,776, 1994.
- [49] M. Fourar, R. Lenormand, M. Karimi-Fard, and R. Horne. Inertia effects in high-rate flow through heterogeneous porous media. *Transport in Porous Media*, 60(3):353–370, 2005.
- [50] F. Thauvin and K. K. Mohanty. Network modeling of non-Darcy flow through porous media. *Transport in Porous Media*, 31(1):19–37, 1998.
- [51] E. Skjetne and J. L. Auriault. High-velocity laminar and turbulent flow in porous media. *Transport in Porous Media*, 36(2):131–147, 1999.
- [52] C. C. Mei and J. L. Auriault. The effect of weak inertia on flow through a porous-medium. *Journal of Fluid Mechanics*, 222:647–663, 1991.
- [53] S. J. Liu, A. Afacan, and J. Masliyah. Steady incompressible laminar-flow in porous media. *Chemical Engineering Science*, 49(21):3565–3586, 1994.
- [54] D. L. Koch and R. J. Hill. Inertial effects in suspension and porous-media flows. *Annual Review of Fluid Mechanics*, 33:619–647, 2001.

- [55] R. J. Hill, D. L. Koch, and A. J. C. Ladd. The first effects of fluid inertia on flows in ordered and random arrays of spheres. *Journal of Fluid Mechanics*, 448:213–241, 2001.
- [56] R. J. Hill, D. L. Koch, and A. J. C. Ladd. Moderate-Reynolds-number flows in ordered and random arrays of spheres. *Journal of Fluid Mechanics*, 448:243–278, 2001.

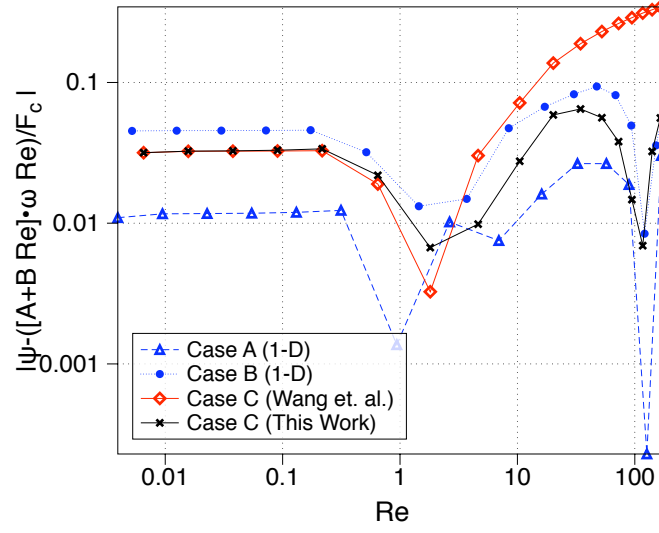
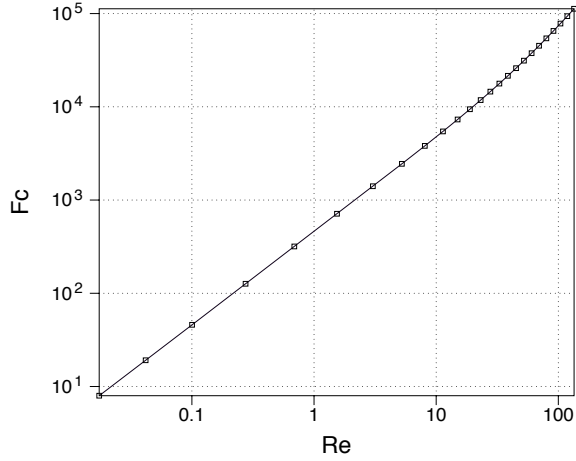
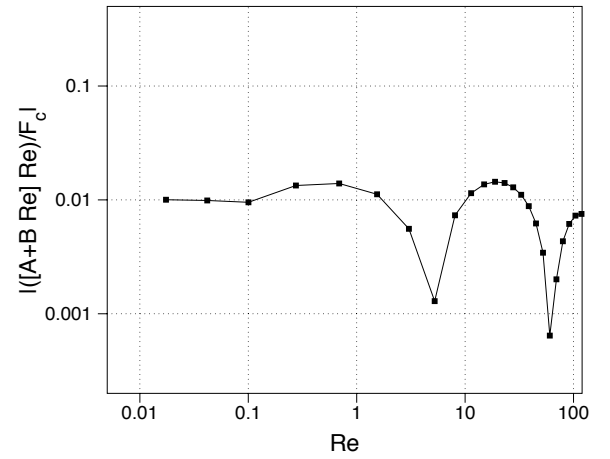


FIG. 4: (Color online) Relative error associated with various predictive forms plotted as a function of Re . Accurate prediction of three-dimensional flow behavior requires all coefficients appearing in Eq. (11).



(a) F_c plotted as a function of Re .



(b) Relative error associated with the predictive form plotted as a function of Re where $a^* = 452.75$ and $b^* = 2.811$.

FIG. 5: Simulated data points and best-fit curve for an isotropic sphere pack with a porosity of 0.37.

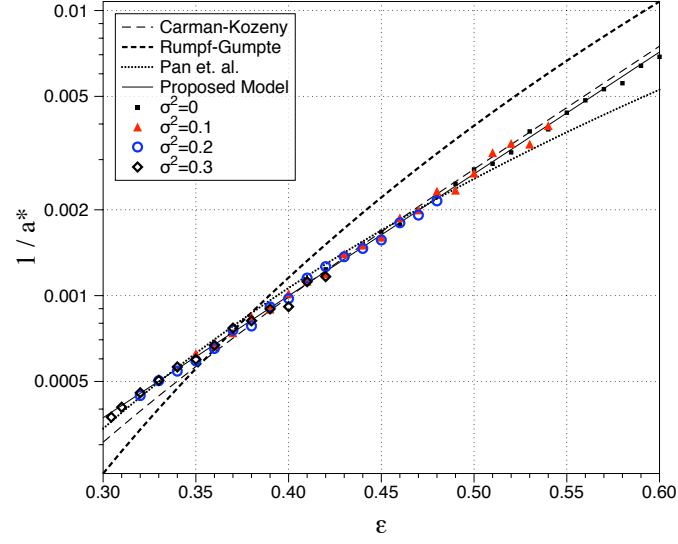


FIG. 6: (Color online) Comparison of isotropic constitutive laws that predict a^* with simulated data.

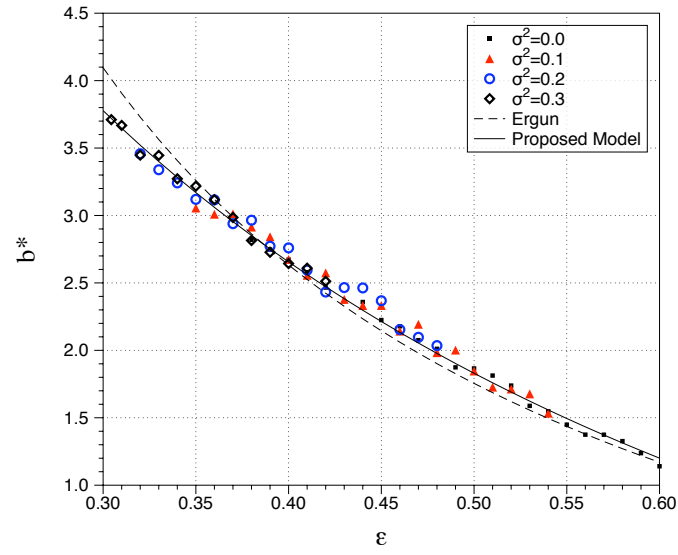


FIG. 7: (Color online) Comparison of isotropic constitutive laws that predict b^* with simulated data.

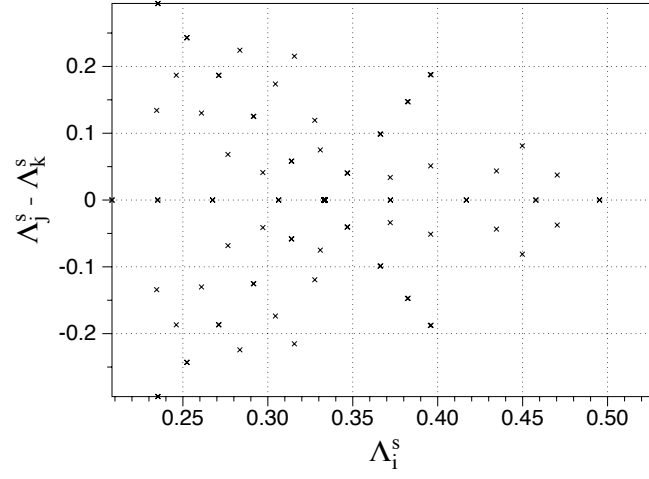
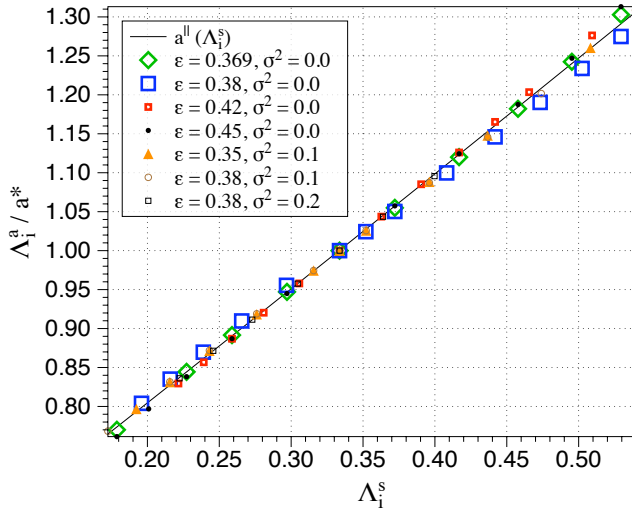
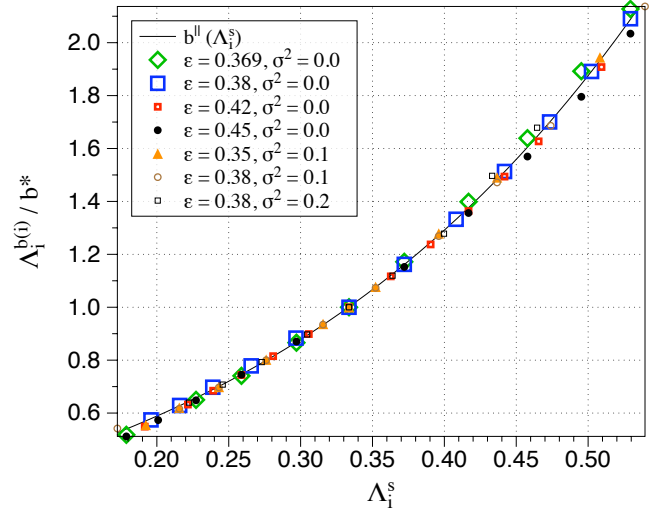


FIG. 8: Domain range for the two independent components of the orientation tensor considered in the constitutive laws.



(a)



(b)

FIG. 9: (Color online) Anisotropic simulation data and best-fit functional forms for $\alpha^{\parallel}(\Lambda_i^s)$ and $\beta^{\parallel}(\Lambda_i^s)$.

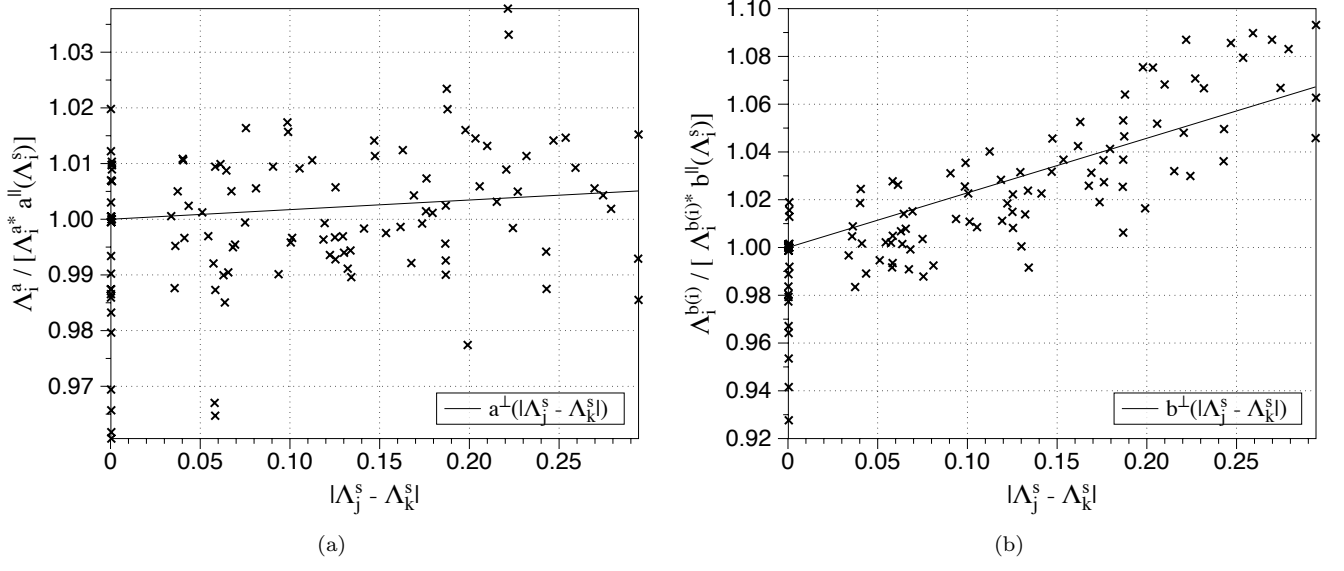


FIG. 10: Anisotropic simulation data plotted with best-fit functional forms for $a^{\perp}(|\Lambda_j^s - \Lambda_k^s|)$ and $b^{\perp}(|\Lambda_j^s - \Lambda_k^s|)$.

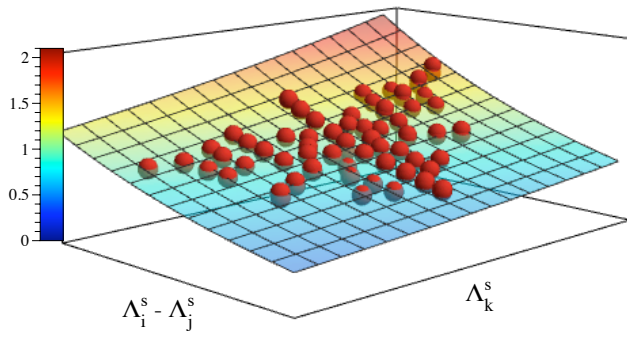


FIG. 11: (Color online) Anisotropic simulation data with surface determined by best-fit functional forms $b^{\dagger}(\Lambda_i^s - \Lambda_j^s)b^{\ddagger}(\Lambda_k^s)$